Extreme Mechanics Letters 44 (2021) 101211

Contents lists available at ScienceDirect

Extreme Mechanics Letters

journal homepage: www.elsevier.com/locate/eml

Morphological changes of nanofiber cross-sections due to surface tension

Shuang Wang [a], Xiying Li [a], Xin Yi [a,*], Huiling Duan [a,b,*]

[a] Department of Mechanics and Engineering Science, Beijing Innovation Center for Engineering Science and Advanced Technology, College of Engineering, Peking University, Beijing 100871, PR China

[b] CAPT, HEDPS and IFSA, Collaborative Innovation Center of the Ministry of Education, State Key Laboratory for Turbulence and Complex System, Peking University, Beijing 100871, PR China

ARTICLE INFO

Article history:
Received 3 December 2020
Received in revised form 13 January 2021
Accepted 1 February 2021
Available online 6 February 2021

Keywords:
Surface tension
Gurtin–Murdoch model
Small-scale soft fibers
Morphological changes
Complex variables formulation

ABSTRACT

In the manufacturing of soft fibers at small scales, lack of considering the presence of surface tension may cause a significant shape deviation from the desired geometry due to the surface tension-induced fiber deformation. Here we develop an analytic algorithm to calculate the surface tension-induced deformation of soft nanofibers with different cross-section shapes. We prove that the displacement at the fiber cross-section boundary is independent of the cross-section size. Numerical examples demonstrate that upon surface tension nanofibers with circular cross-sections undergo radial shrinking and these with non-circular cross-sections are driven to rounder shapes. Moreover, the surface tension-induced cross-section area change is significant for non-circular soft nanofibers as their sizes fall below tens of nanometers.

1. Introduction

Surface stress effects play key roles in regulating mechanical behaviors of solid materials at small scales [1]. One of the widely adopted continuum models incorporating the surface stress on solid deformation is the Gurtin–Murdoch model, in which both the residual surface tension and strain-dependent surface elasticity are taken into account. Mounting analysis has been performed on the mechanical behaviors of nanostructured materials based on the Gurtin–Murdoch model, such as the stress state of nanosized hole/void/cavity [2–6] and inclusions [7–10], effective elastic constants of nanostructured materials [11], crack problems incorporating surface effects [12], vibration and instability of nanobeams [13], and nanoindentation of soft layers [14]. In comparison with extensive efforts devoted to the stress-related analysis of nanomaterials, much less attention has been paid to the analysis of nanomaterial deformation and morphological changes. A possible reason could be that most of the relevant works are focusing on hard materials, such as metals, wherein the deformation induced by the surface stress is significantly small due to the high material stiffness (up to tens of GPa, see, e.g., [7]). For example, the radial and hoop strains on the surface of a spherical void with a radius of 5 nm in a freshly cleaved iron are smaller than 0.1% [2]. The interfacial residual tension and interfacial elasticity barely affect the equilibrium shape of Ni_3Al precipitates with misfit eigenstrains in Ni–Al matrix [15]. Moreover, it has been pointed out that the effect of surface stress on the dynamics of interface/surface evolution is relatively small in most cases, and can be neglected in analyzing the instabilities of core–shell heterostructured cylinders with high stiffness [16].

With the rapidly growing attention to soft robotics and flexible structures at small scales, significant attention has been drawn to the mechanical behaviors of soft nanostructures influenced by the surface stress, such as the surface tension-induced stiffening of a soft matrix by microsize liquid inclusions [17], Rayleigh–Plateau instability in soft elastic filaments [18], and the stress concentration around an elliptic hole inside a soft matrix [19]. Owing to the low stiffness of soft materials (e.g., Young's modulus of silicone gels could be merely 1.7 kPa [17]), the surface stress can cause evident deformation [20]. Consequently, the morphology of small-scale soft materials in manufacturing may deviate significantly from the desired shape with a lack of careful consideration of the surface stress effect.

Understanding the mechanical deformation of soft materials at a small scale is fundamentally important to the rational design and control of soft structures. In this theoretical work, we focus on the morphological changes of soft fibers induced by surface tension under plane strain deformation. Nanofibers of various cross-section shapes are considered. Employing Muskhelishvili's complex variable formulation for plane elasticity [21], we obtain the cross-section morphological and area changes of soft nanofibers upon surface tension. Our results indicate that those changes are determined by the cross-section shape and size, elastic constants of nanofibers, and surface tension magnitude.

* Corresponding authors.
E-mail addresses: xyi@pku.edu.cn (X. Yi), hlduan@pku.edu.cn (H.L. Duan).

https://doi.org/10.1016/j.eml.2021.101211
2352-4316/

2. Problem description and complex variable formulation

Consider a long cylindrical soft nanofiber with an arbitrarily shaped cross-section upon surface tension. The fiber is made of an isotropic linear elastic material. The cross-section of the fiber occupies a simply connected region Ω with a smooth boundary Γ. The local outward unit normal vector $\mathbf{n}$ and unit tangential vector $\mathbf{t}$ of the boundary Γ form the basis of a right-handed local coordinate system nt. The angle between $\mathbf{n}$ and the positive x-axis is α.

The surface tension vector with magnitude γ reads $\boldsymbol{\gamma} = \gamma\mathbf{t}$ at Γ and is related to the bulk stress tensor $\boldsymbol{\sigma}$ at the boundary through the generalized Young–Laplace equation denoting the force balancing [1]

$$\boldsymbol{\sigma}\cdot\mathbf{n} = \frac{\mathrm{d}\gamma}{\mathrm{d}s},$$

where s is the arclength at the fiber cross-section boundary. Then

$$\boldsymbol{\sigma}\cdot\mathbf{n} = \frac{\mathrm{d}(\gamma\mathbf{t})}{\mathrm{d}s} = \gamma\frac{\mathrm{d}\mathbf{t}}{\mathrm{d}s} = \gamma k\mathbf{n} \tag{1}$$

where $k = -\mathrm{d}\alpha/\mathrm{d}s$ is the local curvature. From Eq. (1), we have the normal stress σ_{nn} and shear stress σ_{nt} at the boundary

$$\begin{cases}\sigma_{nn} = \mathbf{n}\cdot\boldsymbol{\sigma}\cdot\mathbf{n} = \gamma k = -\gamma\dfrac{\mathrm{d}\alpha}{\mathrm{d}s},\\ \sigma_{nt} = \mathbf{t}\cdot\boldsymbol{\sigma}\cdot\mathbf{n} = 0.\end{cases} \tag{2}$$

The displacement components u_x and u_y in the xy coordinate system and their corresponding components u_n and u_t in the nt coordinate system can be expressed by two analytic complex potentials $\varphi(z)$ and $\psi(z)$ of the complex variable $z = x + iy$ ($i = \sqrt{-1}$) as [21]

$$\begin{cases}2\mu(u_x + iu_y) = \kappa\varphi(z) - z\overline{\varphi'(z)} - \overline{\psi(z)},\\ 2\mu(u_n + iu_t) = [\kappa\varphi(z) - z\overline{\varphi'(z)} - \overline{\psi(z)}]e^{-i\alpha},\end{cases} \tag{3}$$

where μ is the shear modulus and $\kappa = 3 - 4\nu$ with ν being the Poisson ratio. The overbars represent the complex conjugates and primes denote differentiation with respect to the variable in the parentheses.

In the xy coordinate system, the components of the surface traction exerted on Γ are denoted by X and Y, and they satisfy

$$i\int_{\mathrm{A}}^{\mathrm{B}}(X+iY)\mathrm{d}s = [\varphi(z_0) + z_0\overline{\varphi'(z_0)} + \overline{\psi(z_0)}]\Big|_{\mathrm{A}}^{\mathrm{B}},\quad z_0\in\Gamma, \tag{4}$$

where A and B are the starting and ending points of any counterclockwise directed arc on Γ.

From Eq. (2), we know

$$X + iY = \sigma_{nn}\cos\alpha + i\sigma_{nn}\sin\alpha. \tag{5}$$

Inserting Eq. (5) into Eq. (4) leads to [22,23]

$$\varphi(z_0) + z_0\overline{\varphi'(z_0)} + \overline{\psi(z_0)} = -\gamma e^{i\alpha},\quad z_0\in\Gamma, \tag{6}$$

where the integral constant has been omitted. The analytic potentials $\varphi(z)$ and $\psi(z)$ can be determined from Eq. (6) for nanofibers of given cross-section shapes.

3. Problem solutions

For the fiber of an arbitrary cross-section shape, a new variable ζ is introduced such that the complex variables z and ζ are related via the following conformal mapping [21]

$$z = \omega(\zeta) = R\left(\zeta + \sum_{n=1}^{\infty} m_n\zeta^{-n}\right), \tag{7}$$

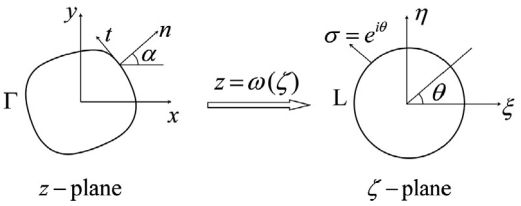

Fig. 1. Schematic of conformal mapping.

through which the exterior of Γ in the physical z-plane is mapped onto the exterior of a unit circle with boundary L in the imaginary ζ-plane and Γ onto L (see Fig. 1). Here the constant R (>0) defines the cross-section size and complex constants $m_n (n = 1, 2\ldots)$ define the cross-section shape. As Γ is mapped onto L, there exists $z_0 = \omega(\sigma) = \omega(e^{i\theta})$ or $\sigma = e^{i\theta} = \sigma(z_0)$ where z_0 and σ denote points on Γ and L, respectively. Note that σ here is different from the stress tensor $\boldsymbol{\sigma}$ and the stress components with subscripts. In practical calculations, the infinite terms of the polynomial (7) are usually truncated with finite terms.

The analytic functions $\varphi(z)$ and $\psi(z)$ in the simply connected region Ω can be expanded and truncated as [24,25]

$$\varphi(z) = \sum_{k=1}^{N} a_k P_k^*(z),\quad \psi(z) = \sum_{k=1}^{N} b_k P_k^*(z), \tag{8}$$

where a_k, b_k are unknown coefficients, and $P_k^*(z)$ are Faber polynomials. On the boundary Γ, the Faber polynomials can be expressed as [24,25]

$$P_k^*(z_0) = P_k^*(\omega(\sigma)) = P_k(\sigma) = \sigma^k + \sum_{n=1}^{\infty}\beta_{k,n}\sigma^{-n}, \tag{9}$$

where the coefficients $\beta_{k,n}$ $(k, n = 1, 2, \ldots)$ are determined through the following relations

$$\beta_{1,n} = m_n,$$

$$\beta_{k+1,n} = m_{k+n} + \beta_{k,n+1} + \sum_{i=1}^{n} m_{n-i}\beta_{k,i} - \sum_{i=1}^{k} m_{k-i}\beta_{i,n}$$

with coefficients m_n, m_{k+n}, m_{n-i} and m_{k-i} taken from Eq. (7).

Inserting Eqs. (8) and (9) into Eq. (6) results in

$$\sum_{k=1}^{N}\left[a_k P_k(\sigma) + \overline{a_k}\frac{\omega(\sigma)}{\overline{\omega'(\sigma)}}\overline{P_k'(\sigma)} + \overline{b_k P_k(\sigma)}\right] = -\gamma\sigma\frac{\omega'(\sigma)}{|\omega'(\sigma)|}. \tag{10}$$

Here we have used the expression $e^{i\alpha} = \sigma\omega'(\sigma)/|\omega'(\sigma)|$.

Using the following truncated Fourier series expansions

$$P_k(\sigma) = \sum_{n=-N}^{N} C_{n1}^k\sigma^n,\qquad \frac{\omega(\sigma)}{\overline{\omega'(\sigma)}}\overline{P_k'(\sigma)} = \sum_{n=-N}^{N} C_{n2}^k\sigma^n,$$

$$\overline{P_k(\sigma)} = \sum_{n=-N}^{N} C_{n3}^k\sigma^n,\qquad \sigma\frac{\omega'(\sigma)}{|\omega'(\sigma)|} = \sum_{n=-N}^{N} C_{n4}\sigma^n$$

with

$$C_{n1}^k = \frac{1}{2\pi}\int_0^{2\pi} P_k(\sigma)\sigma^{-n}\mathrm{d}\theta,\quad C_{n2}^k = \frac{1}{2\pi}\int_0^{2\pi}\frac{\omega(\sigma)}{\overline{\omega'(\sigma)}}\overline{P_k'(\sigma)}\sigma^{-n}\mathrm{d}\theta,$$

$$C_{n3}^k = \frac{1}{2\pi}\int_0^{2\pi}\overline{P_k(\sigma)}\sigma^{-n}\mathrm{d}\theta,\quad C_{n4} = \frac{1}{2\pi}\int_0^{2\pi}\sigma\frac{\omega'(\sigma)}{|\omega'(\sigma)|}\sigma^{-n}\mathrm{d}\theta,$$

Eq. (10) becomes

$$\sum_{n=-N}^{N}\left[\sum_{k=1}^{N} a_k C_{n1}^k + \overline{a_k}C_{n2}^k + \overline{b_k}C_{n3}^k\right]\sigma^n = \sum_{n=-N}^{N}(-\gamma)C_{n4}\sigma^n. \tag{11}$$

From Eq. (11) one can obtain $2N$ linear equations with $2N$ unknown coefficients a_k and $b_k\,(k = 1, \ldots, N)$ as

$$\sum_{k=1}^{N} a_k C_{n1}^k + \overline{a_k} C_{n2}^k + \overline{b_k} C_{n3}^k = -\gamma C_{n4}, \quad n = -N, \ldots, -1, 1, \ldots, N. \tag{12}$$

Solving a_k and b_k $(k = 1, \ldots, N)$ from Eq. (12), the complex potentials $\varphi(z)$ and $\psi(z)$ can be determined from Eq. (8), and the displacement components are determined from Eq. (3).

4. Results and discussion

The following desired cross-section shapes (after deformation) are considered [21] (Fig. 2)

$$\begin{cases} z = \omega(\zeta) = R\zeta, & \text{circle with radius } R, \\ z = \omega(\zeta) = R(\zeta + \zeta^{-1}/2), & \text{ellipse with aspect ratio 1/3}, \\ z = \omega(\zeta) = R(\zeta + \zeta^{-2}/3), & \text{approximate equilateral triangle}, \\ z = \omega(\zeta) = R(\zeta + \zeta^{-3}/6), & \text{approximate square}. \end{cases} \tag{13}$$

For a nanofiber of circular cross-section with a radius R, the displacement components in the nt coordinate system can be obtained as

$$u_n = -\frac{(\kappa - 1)\gamma}{4\mu}\frac{\rho}{R} < 0, \qquad u_t = 0, \tag{14}$$

where ρ is the distance from the section origin. Eq. (14) agrees with analytical results in Ref. [26]. From Eq. (14), one can find that the boundary displacement is $u_n|_{\rho=R} = -(\kappa - 1)\gamma/(4\mu)$, independent of the cross-section size. This result can also be derived from a simple plane elasticity analysis as follows. In the case of a circular cross-section, the uniform surface tension γ is equivalent to a uniform pressure $p = -\gamma/R$ according to the Young–Laplace equation, and the resulting normal stress components in the radial and circumferential directions are $\sigma_{rr} = \sigma_{\theta\theta} = p$ with vanishing shearing-stress component in a polar coordinate whose origin is located at the section center. Therefore, a uniform strain in the radial direction is obtained as $\varepsilon_{rr} = [(1 - \nu)\sigma_{rr} - \nu\sigma_{\theta\theta}]/(2\mu) = (\kappa - 1)p/(4\mu R)$ or equivalently the radial displacement $u_r = u_n$ in Eq. (14).

For nanofibers with non-circular cross-sections, the displacement field can be expressed by (truncated) series expansions. The number N of the truncated series terms is determined by the criterion that the relative error between two consecutive sums of the series is smaller than 0.1%. In the present work, $N = 60$ is a good choice. For all numerical calculations, we take material constants as [19]

$$\gamma = 0.019\,\text{N/m}, \ \mu = 256.84 \times 10^3\,\text{Pa}, \ \nu = 0.499.$$

Fig. 2 demonstrates the surface tension-induced morphological changes of nanofibers with circular, elliptic, triangular, and square cross-sections. It is found that the nanofiber of a circular cross-section undergoes radial shrinking while nanofibers of non-circular cross-sections shrink remarkably in the regions of relatively large curvatures but inflate slightly in the regions of relatively small curvatures. This curvature-mediated deformation feature leads to a more significant change of cross-section area for non-circular cross-sections in comparison with circular cross-sections (Fig. 3). We also calculate the variance of distances between the boundary points and section origin after and before the nanofiber deformation, and find that the ratio of the distance variances after and before deformation for the elliptic, triangular, and square cross-sections are 0.11, 0.083, and 0.047, respectively, significantly smaller than 1. In this sense, the surface tension drives non-circular cross-sections to a rounder geometry [17,27].

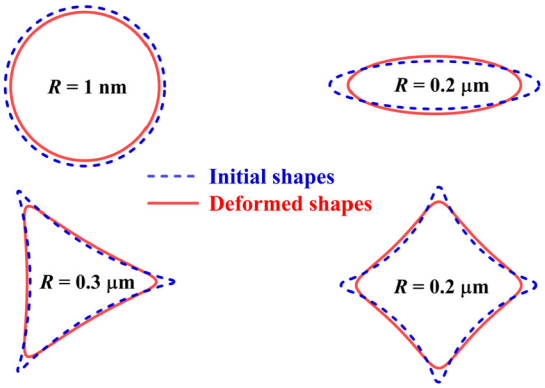

Fig. 2. Morphological changes of selected nanofiber cross-sections.

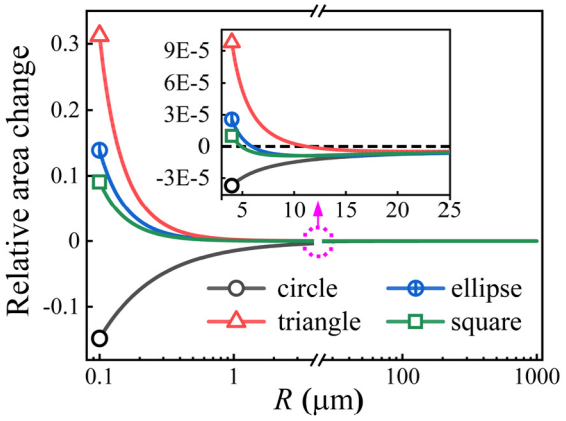

Fig. 3. Relative area changes of different fiber cross-sections as functions of R. Data for the circular fiber have been enlarged 100 times for a clearer comparison.

Fig. 3 shows the relative area change of the cross-section (cross-section area change divided by initial area). The areas of nanofibers with circular cross-sections always decrease, which is also reflected in Eq. (14) with a negative radial displacement. For nanofibers with non-circular cross-sections, however, the cross-section areas may, surprisingly, increase dramatically when the cross-section size falls below tens of nanometers.

The different features of nanofibers with circular and elliptic cross-sections in Fig. 4 indicate that the aspect ratio plays an important role in regulating the morphological changes due to surface tension. To further investigate the aspect ratio effect, we examine the relative area changes versus aspect ratio m, defined as the ratio between the semi-minor axis length and semi-major axis length (Fig. 4). The cross-section area is fixed as πR_0^2, where R_0 is the radius of the circular cross-section. At a given R_0, the relative area change decreases as m increases. Moreover, there exist size-dependent critical aspect ratios, below which areas of the deformed nanofibers with elliptic cross-sections become larger than the initial areas.

To investigate the surface tension effect, we introduce a dimensionless parameter $\gamma/(\mu R)$ which is usually no more than 10^{-1} for solid materials [28]. Fig. 5 depicts the horizontal displacement components of the rightmost points u_x/R (their vertical displacement components are zero due to symmetry) versus the dimensionless surface tension $\gamma/(\mu R)$. From Fig. 5, one can see that u_x/R decreases linearly with $\gamma/(\mu R)$ and the slope

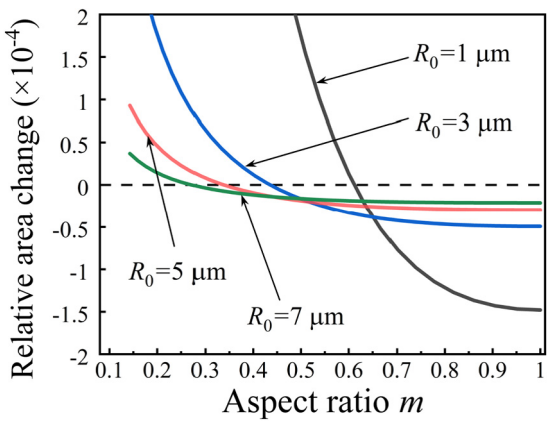

Fig. 4. Relative area changes as functions of aspect ratio m for nanofibers with elliptic cross-sections.

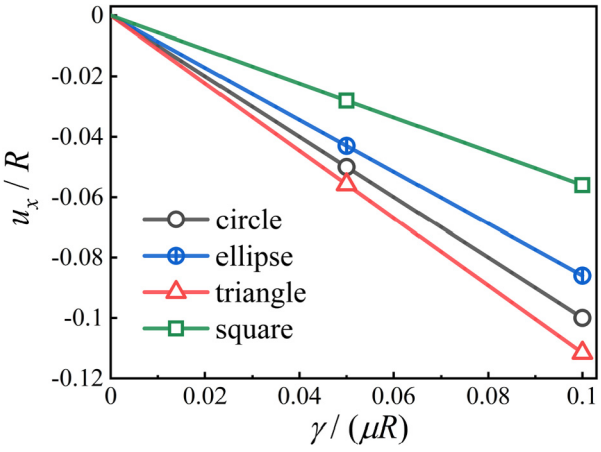

Fig. 5. Normalized displacement u_x at the rightmost points of the nanofibers versus normalized surface tension. The results for the circular fiber have been enlarged 100 times for a clearer comparison.

$-\mathrm{d}u_x/\mathrm{d}(\gamma/\mu)$ depends on the cross-section shape. Moreover, the linear relationship between u_x/R and $\gamma/(\mu R)$ indicates that u_x of the rightmost points is independent of R. Below we give a proof to show that this conclusion holds for arbitrary cross-section shape. The boundary displacement components are related to the complex potentials via Eq. (3)

$$2\mu(u_x + iu_y)\big|_\Gamma = \kappa\varphi(z_0) - z_0\overline{\varphi'(z_0)} - \overline{\psi(z_0)}, \quad z_0 \in \Gamma. \tag{15}$$

Moreover, the boundary condition (6) that determines the complex potentials reads

$$\varphi(z_0) + z_0\overline{\varphi'(z_0)} + \overline{\psi(z_0)} = -\gamma e^{i\alpha} = -\gamma\sigma\frac{\omega'(\sigma)}{|\omega'(\sigma)|}, \quad z_0 \in \Gamma, \tag{16}$$

which is only related to the cross-section shape. Therefore, the boundary displacement components $(u_x + iu_y)\big|_\Gamma$ are independent of the cross-section size.

For an arbitrary shape with a simple-closed boundary curve Γ, the Riemann mapping theorem [29] indicates that there exists a unique conformal mapping from the exterior of Γ onto the exterior of the unit circle with boundary L, and from Γ onto L. With knowledge of the conformal mapping (for example, Eqs. (7) and (13) in our case studies), the morphological change of a nanofiber with arbitrary cross-section shape can be obtained following the presented scheme in Section 3.

5. Conclusions

Based on the complex variable formulation, we have investigated the morphological changes and geometrical properties for soft nanofibers upon surface tension. Nanofibers of circular, elliptic, triangular, and square cross-section shapes are analyzed. For a nanofiber with circular cross-section, the radius always shrinks and the cross-section area always decreases upon surface tension. For nanofibers with non-circular cross-sections, the surface tension drives the cross-sections to rounder geometries and the cross-section areas may significantly increase as their sizes fall below some critical values. Moreover, it is found that the displacement at the cross-section boundary linearly depends on the surface tension but is independent of the cross-section size. The present work is based on the linear elasticity theory and cannot be simply employed to address large deformation.

CRediT authorship contribution statement

Shuang Wang: Conceptualization, Modeling, Software, Data collection, Analysis, Visualization, Writing - original draft, Writing - review & editing, Funding acquisition. **Xiying Li:** Validation, Analysis, Visualization, Writing - original draft. **Xin Yi:** Conceptualization, Analysis, Writing - review & editing, Project administration, Supervision, Funding acquisition. **Huiling Duan:** Conceptualization, Analysis, Writing - review & editing, Project administration, Supervision, Funding acquisition.

Declaration of competing interest

The authors declare that they have no known competing financial interests or personal relationships that could have appeared to influence the work reported in this paper.

Acknowledgments

This work was supported by the National Natural Science Foundation of China (Grant Nos. 11988102, 11872004 and 12002004). Computation resources supported by the High-performance Computing Platform of Peking University are acknowledged.

References

[1] M.E. Gurtin, A.I. Murdoch, A continuum theory of elastic material surfaces, Arch. Ration. Mech. Anal. 57 (1975) 291–323, https://doi.org/10.1007/BF00261375.
[2] L.H. He, Z.R. Li, Impact of surface stress on stress concentration, Int. J. Solids Struct. 43 (2006) 6208–6219, https://doi.org/10.1016/j.ijsolstr.2005.05.041.
[3] G.F. Wang, T.J. Wang, Deformation around a nanosized elliptical hole with surface effect, Appl. Phys. Lett. 89 (2006) 161901, https://doi.org/10.1063/1.2362988.
[4] S. Wang, S.C. Xing, Z.T. Chen, C.F. Gao, A nanoscale hole of arbitrary shape with surface elasticity, J. Elasticity 136 (2019) 123–135, https://doi.org/10.1007/s10659-018-9700-7.
[5] S. Wang, C.F. Gao, Z.T. Chen, Interaction between two nanoscale elliptical holes with surface tension, Math. Mech. Solids 24 (2019) 1556–1566, https://doi.org/10.1177/1081286518801051.
[6] H.B. Yang, M. Dai, Influence of surface roughness on the stress field around a nanosized hole with surface elasticity, Z. Angew. Math. Phys. 69 (2018) 127, https://doi.org/10.1007/s00033-018-1022-x.
[7] L. Tian, R.K.N.D. Rajapakse, Elastic field of an isotropic matrix with a nanoscale elliptical inhomogeneity, Int. J. Solids Struct. 44 (2007) 7988–8005, https://doi.org/10.1016/j.ijsolstr.2007.05.019.
[8] S.G. Mogilevskaya, S.L. Crouch, H.K. Stolarski, Multiple interacting circular nano-inhomogeneities with surface/interface effects, J. Mech. Phys. Solids 56 (2008) 2298–2327, https://doi.org/10.1016/j.jmps.2008.01.001.
[9] H.B. Yang, S. Wang, Interface tension-induced stress field around periodic nano-inclusions of arbitrary shape, Math. Mech. Solids 24 (2019) 2844–2857, https://doi.org/10.1177/1081286518820084.

[10] S. Wang, Z.T. Chen, C.F. Gao, Analytic solution for a circular nano-inhomogeneity in a finite matrix, Nano Mater. Sci. 1 (2019) 116–120, https://doi.org/10.1016/j.nanoms.2019.02.002.
[11] H.L. Duan, J. Wang, Z.P. Huang, B.L. Karihaloo, Size-dependent effective elastic constants of solids containing nano-inhomogeneities with interface stress, J. Mech. Phys. Solids 53 (2005) 1574–1596, https://doi.org/10.1016/j.jmps.2005.02.009.
[12] C.I. Kim, P. Schiavone, C.Q. Ru, Analysis of plane-strain crack problems (Mode-I & Mode-II) in the presence of surface elasticity, J. Elasticity 104 (2011) 397–420, https://doi.org/10.1007/s10659-010-9287-0.
[13] R. Ansari, R. Gholami, A. Norouzzadeh, M.A. Darabi, Surface stress effect on the vibration and instability of nanoscale pipes conveying fluid based on a size-dependent timoshenko beam model, Acta Mech. Sin. 31 (2015) 708–719, https://doi.org/10.1007/s10409-015-0435-4.
[14] M. Li, H.X. Zhang, Z.L. Zhao, X.Q. Feng, Surface effects on cylindrical indentation of a soft layer on a rigid substrate, Acta Mech. Sin. 36 (2020) 422–429, https://doi.org/10.1007/s10409-020-00941-8.
[15] X.J. Zhao, R. Duddu, S.P.A. Bordas, J.M. Qu, Effects of elastic strain energy and interfacial stress on the equilibrium morphology of misfit particles in heterogeneous solids, J. Mech. Phys. Solids 61 (2013) 1433–1445, https://doi.org/10.1016/j.jmps.2013.01.012.
[16] H.L. Duan, J. Weissmüller, Y. Wang, Instabilities of core–shell heterostructured cylinders due to diffusions and epitaxy: Spheroidization and blossom of nanowires, J. Mech. Phys. Solids 56 (2008) 1831–1851, https://doi.org/10.1016/j.jmps.2007.11.009.
[17] R.W. Style, R. Boltyanskiy, B. Allen, K.E. Jensen, H.P. Foote, J.S. Wettlaufer, E.R. Dufresne, Stiffening solids with liquid inclusions, Nat. Phys. 11 (2015) 82–87, https://doi.org/10.1038/nphys3181.
[18] D.L. Henann, K. Bertoldi, Modeling of elasto-capillary phenomena, Soft Matter 10 (2014) 709–717, https://doi.org/10.1039/C3SM52583J.
[19] M. Dai, H.B. Yang, P. Schiavone, Stress concentration around an elliptical hole with surface tension based on the original Gurtin–Murdoch model, Mech. Mater. 135 (2019) 144–148, https://doi.org/10.1016/j.mechmat.2019.05.009.
[20] A. Chakrabarti, M.K. Chaudhury, Direct measurement of the surface tension of a soft elastic hydrogel: Exploration of elastocapillary instability in adhesion, Langmuir 29 (2013) 6926–6935, https://doi.org/10.1021/la401115j.
[21] N.I. Muskhelishvili, *Some Basic Problems of the Mathematical Theory of Elasticity*, Springer, Dordrecht, 1977, https://doi.org/10.1007/978-94-017-3034-1.
[22] M. Dai, P. Schiavone, C.F. Gao, Uniqueness of neutral elastic circular nano-inhomogeneities in antiplane shear and plane deformations, J. Appl. Mech. 83 (2016) 101001, https://doi.org/10.1115/1.4034118.
[23] M. Dai, Y.J. Wang, P. Schiavone, Integral-type stress boundary condition in the complete Gurtin–Murdoch surface model with accompanying complex variable representation, J. Elasticity 134 (2019) 235–241, https://doi.org/10.1007/s10659-018-9695-0.
[24] J.H. Curtiss, Faber polynomials and the faber series, Am. Math. Mon. 78 (1971) 577–596, https://doi.org/10.1080/00029890.1971.11992813.
[25] J.C. Luo, C.F. Gao, Faber series method for plane problems of an arbitrarily shaped inclusion, Acta Mech. 208 (2009) 133–145, https://doi.org/10.1007/s00707-008-0138-z.
[26] M.E. Gurtin, A.I. Murdoch, Surface stress in solids, Int. J. Solids Struct. 14 (1978) 431–440, https://doi.org/10.1016/0020-7683(78)90008-2.
[27] S. Mora, C. Maurini, T. Phou, J.M. Fromental, B. Audoly, Y. Pomeau, Solid drops: Large capillary deformations of immersed elastic rods, Phys. Rev. Lett. 111 (2013) 114301, https://doi.org/10.1103/PhysRevLett.111.114301.
[28] M. Dai, P. Schiavone, C.F. Gao, A new method for the evaluation of the effective properties of composites containing unidirectional periodic nanofibers, Arch. Appl. Mech. 87 (2017) 647–665, https://doi.org/10.1007/s00419-016-1215-8.
[29] P. Hertling, An effective Riemann mapping theorem, Theoret. Comput. Sci. 219 (1999) 225–265, https://doi.org/10.1016/S0304-3975(98)00290-4.